Journal of Materials Chemistry C

ROYAL SOCIETY OF CHEMISTRY

PAPER

View Article Online
View Journal | View Issue

Cite this: J. Mater. Chem. C, 2023, 11, 4603

Chemical vapor deposition growth and photodetector performance of lead-free all-inorganic crystalline $Cs_3Sb_2X_9$ (X = I, Br) perovskite thin films†

Sujit Kumer Shil, *[ab] Fei Wang,[cde] Kingsley O. Egbo,[a] Ying Wang,[a] Cheuk Kai Gary Kwok,[a] Sai-W. Tsang,[c] Johnny C. Ho[cef] and Kin Man Yu*[ac]

Received 12th December 2022,
Accepted 8th March 2023

DOI: 10.1039/d2tc05289j

rsc.li/materials-c

Lead-based organic or inorganic halide perovskites (ABX_3, A = organic or inorganic cation, B = lead cation, and X = Cl, Br, I) are well-known for their excellent properties and are technologically suitable for many optoelectronic devices. However, the stability of organic hybrid compounds and the toxicity of lead (Pb) inhibit the development and commercialization of these devices. Consequently, Pb-free, all-inorganic halide perovskites are now the subject of the recent research interest. In this work, we report on the synthesis and properties of Pb-free all-inorganic $Cs_3Sb_2X_9$ (X = I, Br) perovskite thin films by a two-step CVD approach. The obtained $Cs_3Sb_2I_9$ and $Cs_3Sb_2Br_9$ thin films show good crystallinity and exhibit high exciton binding energies with large Stokes shifts of ~570 and ~630 meV, respectively. Refractive indices of 2.0 and 1.7 were obtained for $Cs_3Sb_2I_9$ and $Cs_3Sb_2Br_9$ thin films at their respective emission energies. The optical bandgaps were confirmed to be 2.2 and 2.85 eV for $Cs_3Sb_2I_9$ and $Cs_3Sb_2Br_9$ thin films. Photoconductive devices fabricated using these thin films exhibit commendable performance with responsivity of up to 54.5 and 3.6 mA W^{-1} and high detectivity reaching 4.3×10^{10} and 1.6×10^{10} Jones for $Cs_3Sb_2I_9$ and $Cs_3Sb_2Br_9$, respectively. Moreover, a stable photoswitching property with fast rise and decay times of 50 ms and 30 ms for $Cs_3Sb_2I_9$ and 108 ms and 56.2 ms for $Cs_3Sb_2Br_9$ film photodetectors was observed. The thin films exhibit excellent long-term stability even when stored without encapsulation in ambient air. The properties of these crystalline $Cs_3Sb_2X_9$ perovskite films and their photodetector performance suggest that they can be promising candidates for a wide range of optoelectronic devices.

Introduction

Lead-based halide perovskites with the chemical formula ABX_3 (A = organic or inorganic cation, B = lead cation, and X = halide anion, Cl, Br, and I) have received great attention because of their outstanding properties such as a large absorption cross-section, high carrier mobility, long diffusion length, low trap-state densities, and long carrier lifetimes. They have been extensively applied in many optoelectronic devices such as solar cells,[1–4] photodetectors,[5–10] lasers,[11,12] light emitting diodes,[13–16] field-effect transistors,[17,18] and photocatalytic CO_2 reduction.[19,20] The first organic hybrid perovskite solar cell (PSC) was reported with a

[a] Department of Physics, City University of Hong Kong, Kowloon, Hong Kong SAR. E-mail: sujit@phy.kuet.ac.bd, kinmanyu@cityu.edu.hk
[b] Department of Physics, Khulna University of Engineering & Technology (KUET), Khulna-9203, Bangladesh
[c] Department of Materials Science and Engineering, City University of Hong Kong, Kowloon, Hong Kong SAR
[d] State Key Laboratory of Luminescence and Applications, Changchun Institute of Optics, Fine Mechanics and Physics, Chinese Academy of Sciences, Changchun 130021, China
[e] State Key Laboratory of Terahertz and Millimeter Waves, City University of Hong Kong, Kowloon, Hong Kong SAR
[f] Key Laboratory of Advanced Materials Processing & Mold (Zhengzhou University), Ministry of Education, Zhengzhou 450002, China

† Electronic supplementary information (ESI) available: Schematic diagrams showing the synthesis of $Cs_3Sb_2X_9$ perovskite thin films by a two-step CVD method. Unit cells and 2D layered structures of $Cs_3Sb_2I_9$ and $Cs_3Sb_2Br_9$ perovskite thin films. XRD spectra of as grown and annealed films. 3D view AFM images of $Cs_3Sb_2I_9$ and $Cs_3Sb_2Br_9$ perovskite thin films. Compositional analysis of $Cs_3Sb_2I_9$ and $Cs_3Sb_2Br_9$ perovskite thin films using XRF spectra. Ellipsometric experimental and simulated spectra of Ψ and Δ for $Cs_3Sb_2I_9$ and $Cs_3Sb_2Br_9$ perovskite thin films. Schematic representation of the surface photovoltage (SPV) in a p-type semiconductor. Schematic diagram and optical image of the $Cs_3Sb_2X_9$ perovskite film photodetector. Photoresponse curves with different illumination power densities and bias voltages. Wavelength dependent photoresponse. Compositional stability after 45 days of storage under ambient conditions. Reproducible on/off response of $Cs_3Sb_2I_9$ and $Cs_3Sb_2Br_9$ film photodetectors after 45 days of storage under ambient conditions, and XRF data with different molar ratios. See DOI: https://doi.org/10.1039/d2tc05289j

low power conversion efficiency (PCE) of 3.5% in 2009.[21] However, only a decade later the PCE of PSCs has surged to over 25.4%, comparable to those of commercial crystalline silicon solar cells.[22]

Irrespective of the remarkable advances achieved in optoelectronic applications, two critical challenges limit the large-scale commercial adoption of these materials. The major challenge is the instability of the material due to the presence of organic cations which are extremely sensitive to oxygen, moisture, and environmental stress.[23–27] This in turn causes the degradation of their device performance over time. Another critical issue is the high toxicity of lead in these materials which raises severe environmental and public health concerns.

To circumvent these challenges, stable all-inorganic and lead-free halide perovskites have become the subject of the current research focus. However, to replace Pb, alternative choices of non-toxic B ions are severely restricted by the narrow range of the Goldschmidt tolerance factor for a close packed stable perovskite structure.[28,29] Structurally similar and equivalent ions to Pb^{2+}, such as Sn^{2+} and Ge^{2+}, have been predicted as suitable replacements for Pb in lead-free perovskites.[30,31] However, the rapid oxidation of Sn^{2+} to Sn^{4+} and Ge^{2+} to Ge^{4+} make the Sn- and Ge-based perovskites highly unstable in ambient air.[29,30]

Recently, defect-based all-inorganic Pb-free perovskites with the formulation $Cs_3M_2X_9$ (M = Bi^{3+} or Sb^{3+} ions) obtained by replacing some of the metal sites by vacancies of conventional ABX_3 perovskites with exceptional stability have been explored.[32–35] The replacement of Pb^{2+} by Bi^{3+} in perovskites generally forms a zero-dimensional molecular structure which increases the effective masses for the free carriers.[35,36] However, several recent studies reported that the power conversion efficiencies for Bi-based inorganic perovskite solar cells were very poor ($<1\%$), which limits their practical photovoltaic applications.[37–39] On the other hand, Sb-based perovskite thin films showed a high absorption coefficient ($>10^5$ cm^{-1}), a nearly direct bandgap and small electron and hole effective masses.[40] The performances of solar cells fabricated using $Cs_3Sb_2I_9$ perovskite thin films synthesized by the solution process have been reported.[33,34] Utilizing the solution-processed layer-form of $Cs_3Sb_2I_9$ thin films, Singh *et al.*[33] obtained a PCE of 1.5%, whereas Umar *et al.*[34] reported a PCE of 1.21%. One of the reasons for the rather low PCE reported in these studies may be the poor quality of the film synthesized by the solution process. Recently, a few works on the solution phase synthesis of $Cs_3Sb_2Br_9$ perovskites with different morphologies such as nanocrystals, quantum dots (QDs), nanoflakes, *etc*. and their optoelectronic applications were reported.[41–44] But to date, a detailed understanding of the fundamental material properties and photoconduction properties of $Cs_3Sb_2X_9$ (I and Br) perovskite thin films is still lacking.

Solution processes for thin film growth have the advantages of being non-vacuum and low cost, but films synthesized by these processes are known to suffer from poor crystalline quality and may contain a high concentration of impurities.[45] Alternatively, chemical vapor deposition (CVD) is a well-recognized technique to grow materials with better crystalline quality and lower defect density. However, due to the large difference in the melting temperature of the precursors, namely CsX (621 °C for CsI and 636 °C for CsBr) and SbX_3 (171 °C for SbI_3 and 96 °C for $SbBr_3$), the synthesis of $Cs_3Sb_2X_9$ perovskite materials using the CVD method is a challenging task. In order to overcome this difficulty, a two-step CVD process was developed and utilized in our previous work to grow $Cs_3Sb_2I_9$ perovskite microplates.[46] The photodetectors fabricated by these CVD synthesized $Cs_3Sb_2I_9$ perovskite microplates achieved an ultra-fast photoresponse with rise and decay times as low as 96 μs and 58 μs, respectively. Hence, we expect that this two-step CVD process can be used to grow thin films as well.

In this work, we carried out a systematic study on the synthesis of all-inorganic and lead-free $Cs_3Sb_2X_9$ (X = I and Br) perovskite thin films using the two-step CVD process. In this two-step CVD process, after the sequential deposition of binary compounds in steps I and II, an annealing process is used to form ternary thin films. The optoelectronic properties of these films are explored and compared with their microplates synthesized by a similar CVD approach. Photoconductive devices are fabricated using these $Cs_3Sb_2X_9$ films, and they show commendable performance with an on/off current ratio of up to 3.43×10^2 (7.32×10^2), a responsivity of up to 54.5 (3.6 mA W^{-1}), and a detectivity of up to 4.3×10^{10} (1.6×10^{10} Jones) for $Cs_3Sb_2I_9$ ($Cs_3Sb_2Br_9$) thin film photodetectors studied with a 532 nm (450 nm) light. Moreover, their rise and decay times can be lowered to 50 ms and 30 ms for $Cs_3Sb_2I_9$ and 108 ms and 56.2 ms for $Cs_3Sb_2Br_9$ film photodetectors, respectively. These results clearly suggest that the two step CVD process is suitable for the synthesis of high quality all-inorganic and lead-free $Cs_3Sb_2X_9$ perovskite thin films and that these films have good potential for high-performance optoelectronic devices.

Results and discussion

$Cs_3Sb_2X_9$ perovskite thin films were synthesized by using a two-step CVD approach in a single zone tube furnace. The detailed synthesis process is illustrated schematically in Fig. S1 in the ESI.† During $Cs_3Sb_2I_9$ growth, the CsI (with a higher melting point of 621 °C) film was first grown in step I under optimized temperature, pressure, and gas flow conditions. Then, the SbI_3 (with a lower melting point of 171 °C) film was grown on top of the CsI film under optimized conditions in step II. Similarly, $Cs_3Sb_2Br_9$ (CsBr in step I and $SbBr_3$ in step II) perovskite films were deposited. The optimized growth conditions for the individual layers were outlined in the Experimental section. In order to ensure the uniform formation of $Cs_3Sb_2X_9$ perovskite thin films, an additional post-growth annealing process is required. Since the melting temperature of CsX is much higher than that of the SbX_3 precursor, the annealing temperature has to be carefully controlled so that the layers grown by the two steps were well mixed but the lower melting point SbX_3 would not preferentially vaporize. The optimum annealing temperatures were

determined through a series of experiments by systematically increasing the annealing temperature from the melting point of SbX_3 to below the melting point of the CsX precursors. During annealing, the SbX_3 precursor melts gradually and diffuses into CsX films. After the recrystallization, the $Cs_3Sb_2X_9$ perovskite crystalline thin films of thickness ~200 nm were achieved on the substrates.

Unit cells and 2D layered structures of $Cs_3Sb_2X_9$ perovskites are shown according to the available crystallographic data[47] in Fig. S2 of the ESI.† It can be seen in Fig. S2 (ESI†) that the unit cells of $Cs_3Sb_2I_9$ and $Cs_3Sb_2Br_9$ perovskites consist of bi-octahedral $(Sb_2I_9)^{3-}$ and $(Sb_2Br_9)^{3-}$ clusters, respectively. For balancing the charge, 10 Cs cations surround the bi-octahedral clusters. Each unit cell holds a trigonal crystal system with the space group of $P\bar{3}m1$ (164). X-ray diffraction (XRD) spectra of the annealed samples reveal high crystallinity of the $Cs_3Sb_2X_9$ perovskite thin films, with diffraction peaks properly indexed to the 2D layered $Cs_3Sb_2I_9$ perovskite (JCPDS No. 88-0690) and $Cs_3Sb_2Br_9$ perovskite structure (JCPDS No. 77-1055), respectively (Fig. 1). A comparison of the XRD spectra of as grown and annealed films are shown in Fig. S3 and S4 (ESI†) which confirmed that post-growth annealing is essential to achieve the right phase of the respective films. The intensities of the XRD spectra suggest that the $Cs_3Sb_2I_9$ and $Cs_3Sb_2Br_9$ perovskite thin films exhibit preferential growth along the <201> direction. More importantly, the X-ray rocking-curve (RC) measurements around the (201) diffraction peaks (shown as insets in Fig. 1) yield small full width at half maximum (FWHM) values of 0.18° for $Cs_3Sb_2I_9$ and 0.17° for $Cs_3Sb_2Br_9$ perovskites, showing that the films have high crystalline quality. Compared to their microplate counterparts we reported previously, grown by the same process, the RC peak widths of the thin films are wider (0.145° and 0.095° for $Cs_3Sb_2I_9$ and $Cs_3Sb_2Br_9$ microplates, respectively).[46,48] This can be understood since the microplates are single crystalline while the thin films have a polycrystalline nature.

The surface morphology of the thin films was studied by scanning electron microscopy (SEM) and atomic force microscopy (AFM) (Fig. 2). The average grain size of both films can be estimated to be ~300–400 nm. 3D view AFM images (Fig. S5, ESI†) show that the films are rather rough, with an average surface roughness of ~54 nm for $Cs_3Sb_2I_9$ and ~84 nm for $Cs_3Sb_2Br_9$ thin films. Along with the high surface roughness, pinholes between grains are also present in high density. This may be the result of the non-uniform overlapping of the microplates formed after annealing at 200 °C for $Cs_3Sb_2I_9$ and 140 °C for $Cs_3Sb_2Br_9$ which are much higher than the melting point of the SbX_3 precursors.

Compositional analysis of the films was done by using X-ray fluorescence spectroscopy (XRF). As displayed in the XRF spectra (Fig. S6, ESI†), the elemental atomic percentage ratios of Cs : Sb : I = 22.2 : 15.6 : 62.2 and Cs : Sb : Br = 21.5 : 12.9 : 65.6 were consistent with the expected 3 : 2 : 9 ratio of $Cs_3Sb_2X_9$ perovskites. This result confirms the chemical stoichiometry of $Cs_3Sb_2X_9$ perovskite films *via* two-step CVD growth.

The optical properties of the perovskite thin films were studied by spectroscopic ellipsometry (SE). The complex dielectric function ($\varepsilon = \varepsilon_1 + i\varepsilon_2$, where ε_1 and ε_2 are the real and imaginary parts of ε, respectively) and complex optical constants ($N = n - ik$, where n is the refractive index and i and k are the extinction coefficients) over a wide photon-energy range

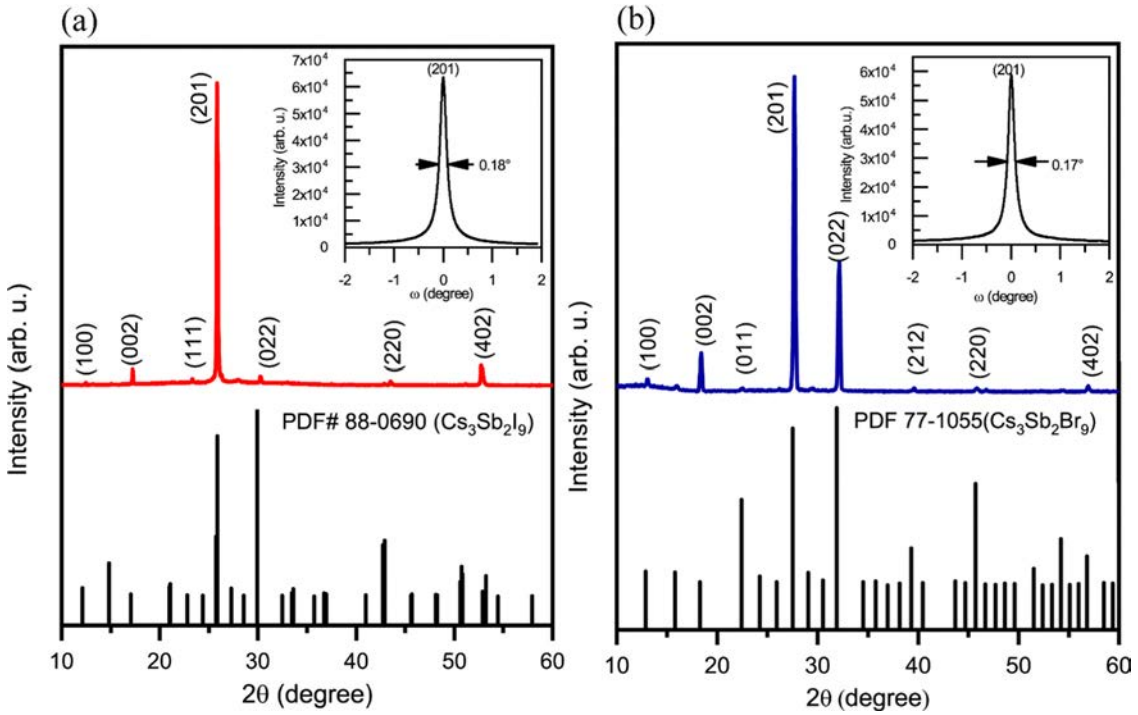

Fig. 1 XRD patterns of the annealed (a) $Cs_3Sb_2I_9$ and (b) $Cs_3Sb_2Br_9$ perovskite thin films. Insets show the (201) rocking curves of the corresponding films.

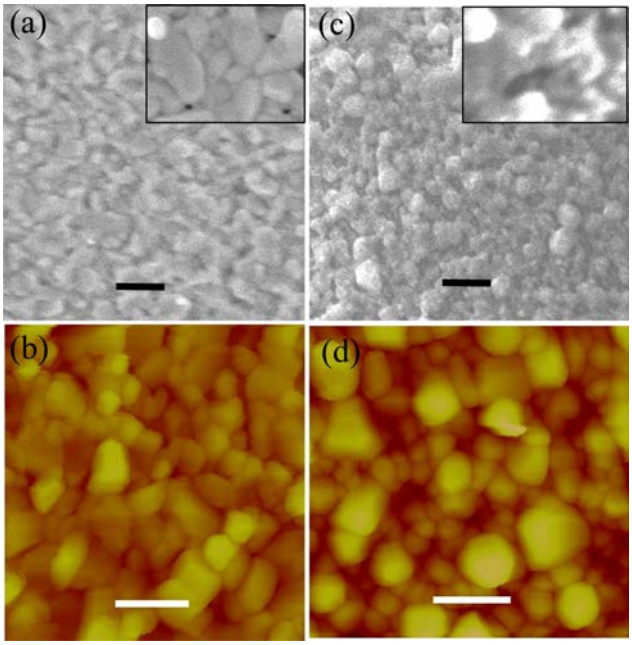

Fig. 2 Surface morphology of $Cs_3Sb_2X_9$ perovskite thin films. Top-view (a) SEM and (b) AFM images of the $Cs_3Sb_2I_9$ thin film. Top-view (c) SEM and (d) AFM images of the $Cs_3Sb_2Br_9$ thin film. Insets show the SEM magnified images of the corresponding films. Scale bars in both the SEM and AFM images are 1 μm.

were obtained by model fitting the SE data using several Tauc–Lorentz (T–L) oscillators. The SE modelling to extract the optical functions and optical constants are outlined in the Experimental section and ESI.†

Experimental and fitted ellipsometric ψ (amplitude) and Δ (phase) spectra of $Cs_3Sb_2X_9$ films are displayed in Fig. S7 and S8 (ESI†). The obtained dielectric function spectra from the model fittings are shown in Fig. 3 (a and b) and the optical constant spectra are shown in Fig. 3(c and d) for the $Cs_3Sb_2X_9$ perovskite thin films. The overall ε spectra of the two films look similar. However, the ε values are higher for the $Cs_3Sb_2I_9$ film than the $Cs_3Sb_2Br_9$ film. The smaller ε, in turn, results in the larger oscillator strength of the excitons in $Cs_3Sb_2Br_9$, which is clearly seen in Fig. 3(a and b). Refractive indices are ~2.2 at an energy of 2.2 eV for $Cs_3Sb_2I_9$ and ~1.8 at an energy of 2.85 eV for $Cs_3Sb_2Br_9$ thin films. In our previous work, the refractive index of $Cs_3Sb_2Br_9$ perovskite microplates was found to be ~2.1 at an energy of 2.85 eV.[46] Generally, the optical constants of single crystal or bulk materials are higher compared to their thin films due to a higher material density and fewer defects from voids and surface inhomogeneity. For instance, Leguy *et al.* reported a refractive index of ~2.45 for $CH_3NH_3PbI_3$ perovskites at 1.55 eV for the single crystal, whereas for the thin films it is considerably lower than ~1.95.[49]

The extinction coefficient k (Fig. 3c and d) shows a very low value and subgap absorption features are not observable at the lower energy range. The absorption coefficient (α) is calculated using the relationship $\alpha = 4\pi k/\lambda$ and is plotted in Fig. 3(e and f). The absorption coefficient spectra show discrete excitonic peaks at ~2.1 eV and ~2.8 eV for the $Cs_3Sb_2Br_9$ and $Cs_3Sb_2I_9$ thin films, respectively. These excitonic peaks are followed at higher energies by a band to band absorption continuum. The bandgaps of the $Cs_3Sb_2I_9$ and $Cs_3Sb_2Br_9$ thin films can be estimated from the absorption continuum to be ~2.2 and ~2.85 eV, respectively. This suggests that both $Cs_3Sb_2I_9$ and $Cs_3Sb_2Br_9$ thin films have a high exciton binding energy (E_b). In particular, for the $Cs_3Sb_2I_9$ thin film, the binding energy can be determined from the difference between the band edge and the exciton edge to be ~250 meV. Similar high E_b values were also obtained for $Cs_3Sb_2I_9$ (230 meV) and $Cs_3Sb_2Br_9$ (200 meV) perovskite microplates synthesized in our previous reports.[46,48] The exciton binding energies obtained for $Cs_3Sb_2X_9$ thin films are much higher than those for Pb-based perovskites (~5–50 meV for $MAPbI_3$ and ~25–70 meV for $MAPbBr_3$[50]) and other semiconductor materials. These high E_b values suggest that these thin films are good candidates for optoelectronic devices that operate under harsh environments such as high temperatures and intense irradiation. However, large E_b values could also lead to the difficulty of exciton dissociation in materials. Therefore, materials with moderate E_b values are more suitable for photon–electron conversion devices. Moreover, a high absorption coefficient of $\sim 1 \times 10^5$ cm^{-1} was observed at an energy of 2.7 eV for the $Cs_3Sb_2I_9$ thin film and at an energy of 3 eV for the $Cs_3Sb_2Br_9$ thin film. This implies that the films can be efficient light absorbers for photovoltaic applications.

Fig. 3(e) and (f) also show the room temperature photoluminescence (PL) emission spectra of $Cs_3Sb_2X_9$ thin films, showing broad and asymmetric PL peaks with peak energies of 1.63 and 2.24 eV for $Cs_3Sb_2I_9$ and $Cs_3Sb_2Br_9$ thin films, respectively. Note that the corresponding band absorption edges are at 2.2 and 2.85 eV, respectively, as shown in Fig. 3(e and f). Umar *et al.* also reported a broad photoluminescence peak and similar peak energy for the $Cs_3Sb_2I_9$ thin film synthesized by a solvent engineering strategy.[34] Compared to the absorption edges, the $Cs_3Sb_2I_9$ and $Cs_3Sb_2Br_9$ thin films exhibit strong Stokes shifts of ~570 and 630 meV, respectively, which are much larger than Stokes shifts observed in other semiconductor materials.[51,52] For instance, typical lead halide perovskites have small Stokes shifts of ~30–70 meV which give rise to a strong self-absorption effect.[51,53] Note that a large Stokes shift is also obtained in our prior reports of $Cs_3Sb_2X_9$ perovskite microplates (~520 meV for $Cs_3Sb_2I_9$ microplates and ~450 meV for $Cs_3Sb_2Br_9$ microplates).[46,48] The large Stokes shifts of $Cs_3Sb_2X_9$ perovskite thin films suggest that they are suitable for light emitting and laser diodes.

To determine the work function and to investigate the electronic structure of the $Cs_3Sb_2X_9$ films, we performed Kelvin probe measurements in the dark and under white light illumination from a QTH (quartz tungsten halogen) light source. For $Cs_3Sb_2I_9$ and $Cs_3Sb_2Br_9$ films, respective work function values of 4.4 and 3.94 eV are obtained in the dark as shown in Fig. 4. Upon illumination, the magnitude of the work function for both films increases, indicating a p-type character of the materials.[54] Note that the change in the work function with light illumination for the $Cs_3Sb_2Br_9$ film (~85 meV) is much

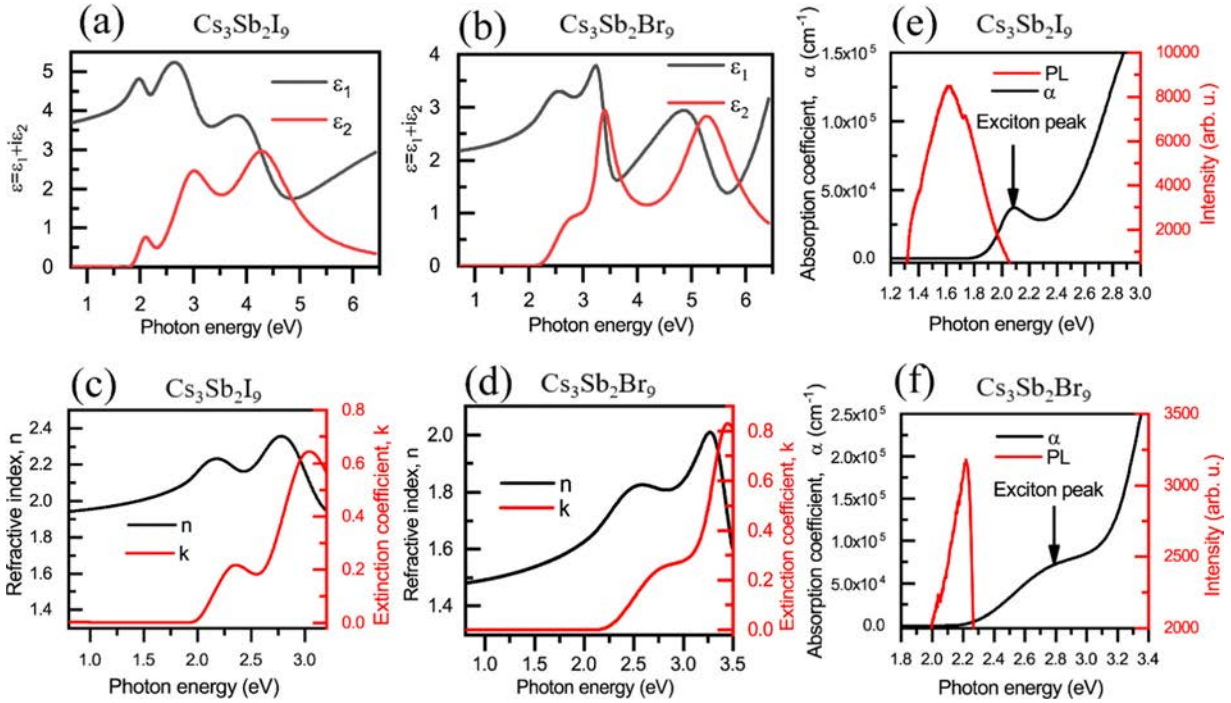

Fig. 3 Optical properties of $Cs_3Sb_2X_9$ perovskite thin films. Real (ε_1) and imaginary (ε_2) parts of the dielectric function ε for (a) $Cs_3Sb_2I_9$ and (b) $Cs_3Sb_2Br_9$ thin films. Energy dependent optical constants (n and k) of (c) $Cs_3Sb_2I_9$ and (d) $Cs_3Sb_2Br_9$ thin films. Steady state photoluminescence spectra along with the absorption spectra of (e) $Cs_3Sb_2I_9$ and (f) $Cs_3Sb_2Br_9$ thin films.

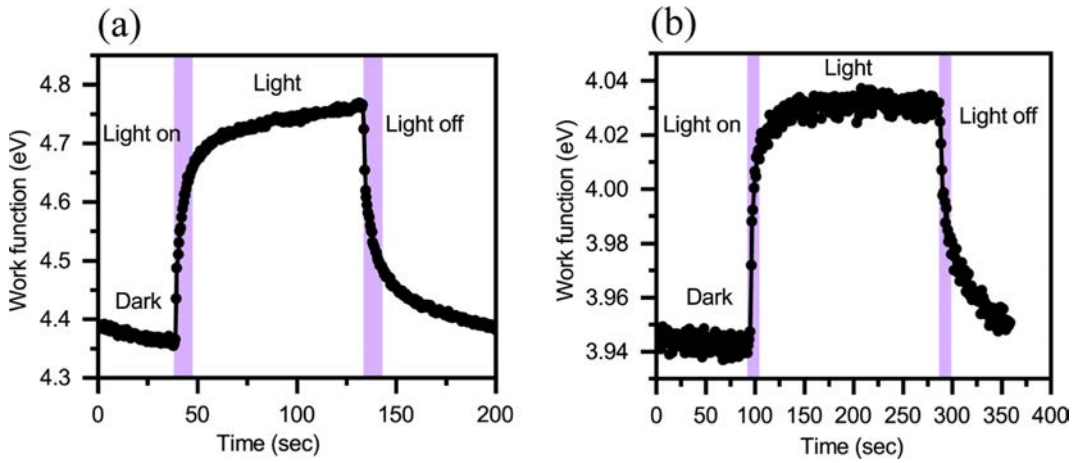

Fig. 4 Surface photovoltage (SPV) measurements of (a) $Cs_3Sb_2I_9$ and (b) $Cs_3Sb_2Br_9$ perovskite thin films.

less than that for the $Cs_3Sb_2I_9$ film ($\sim$300 meV). A schematic diagram of the surface photovoltage (SPV) of a p-type semiconductor is given in the ESI† (Fig. S9). The SPV of $Cs_3Sb_2I_9$ and $Cs_3Sb_2Br_9$ films can be estimated to be 300 and 85 meV, respectively. The low value of SPV is an indication that the surfaces may have a lower density of defects.

To explore the applications of our lead-free perovskite materials, photoconductive devices were fabricated with a metal/semiconductor/metal structure. The schematic diagram and optical image of the fabricated photodetectors are shown in the ESI† (Fig. S10). Fig. 5(a) and (b) show the current–voltage (I–V) characteristics of the $Cs_3Sb_2I_9$ film photodetector in the dark and under the illumination of 532 nm laser light with different incident power densities from 0 to 54 mW cm^{-2}. The $Cs_3Sb_2I_9$ film photodetector exhibits a dark current of around 3.5×10^{-11} A at 2 V, and under illumination the current increases to $\sim 1.2 \times 10^{-9}$ A. Similarly, Fig. 5(c) and (d) show the I–V characteristics of the $Cs_3Sb_2Br_9$ film photodetector in the dark and under the illumination of a 450 nm laser light with different incident power densities from 0 to 70 mW cm^{-2}.

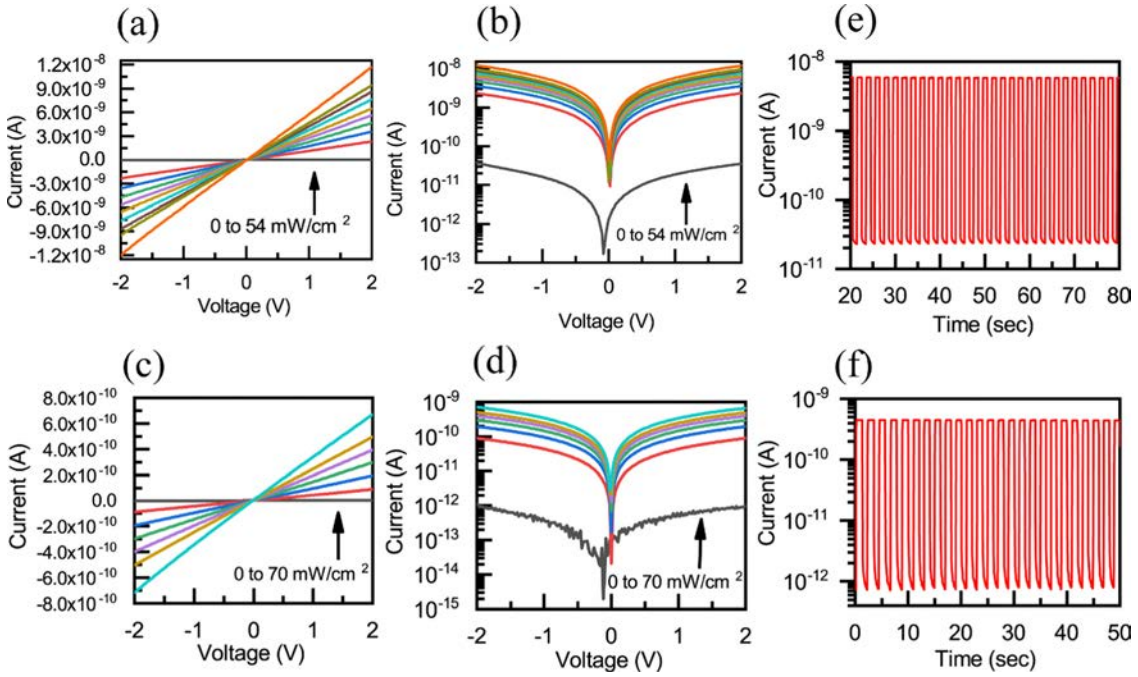

Fig. 5 Photoconductive device characterization. (a) Linear and (b) logarithmic *I–V* characteristics of the $Cs_3Sb_2I_9$ film photodetector in the dark and under the illumination of 532 nm light with different power densities. (c) Linear and (d) logarithmic *I–V* characteristics of the $Cs_3Sb_2Br_9$ film photodetector in the dark and under the illumination of 450 nm light with different power densities. (f) The on/off photoswitching of the (e) $Cs_3Sb_2I_9$ photodetector at an incident power density of 54 mW cm^{-2} and the (f) $Cs_3Sb_2Br_9$ film photodetector at an incident power density of 70 mW cm^{-2}.

The $Cs_3Sb_2Br_9$ film photodetector exhibits a dark current of around 9.7×10^{-13} A at 2 V, and under illumination the current increases to $\sim 7.1 \times 10^{-10}$ A. Note that good ohmic contacts were confirmed with linear *I–V* characteristics between Au electrodes and $Cs_3Sb_2X_9$. The on/off photoswitching property, an important parameter to characterize a photodetector, was measured using a shutter and an excitation source of a 532 nm laser for $Cs_3Sb_2I_9$ and a 450 nm laser for the $Cs_3Sb_2Br_9$ film photodetector. Fig. 5(e) and (f) show the successive on/off switching properties of the devices at 1 V bias. The on/off current ratio can reach up to 3.43×10^2 for $Cs_3Sb_2I_9$ and 7.32×10^2 for $Cs_3Sb_2Br_9$ film photodetectors without any noticeable deterioration in performance over repeated switching cycles. In our previous report, an on/off ratio as high as 10^4 was obtained for a $Cs_3Sb_2I_9$ microplate photodetector.[46] The high on/off ratio value in the microplate photodetector may be due to its single crystalline nature with a higher material density, smooth surfaces and lower defect density. The response time of the film photodetectors was estimated from the on/off photoswitching aspects. The rise time and decay time, the time for the current to increase from 10% to 90% of its peak value and *vice versa*, were determined to be 50 ms, and 30 ms for $Cs_3Sb_2I_9$ and 108 ms and 56.2 ms for the $Cs_3Sb_2Br_9$ film photodetectors as shown in Fig. 6(a) and (b).

To examine the performance stability under both strong and weak signals, the photocurrent of the devices at various illumination power intensities was investigated. Fig. S11 (ESI†) shows that with increasing power intensities, the photocurrent increases proportionally, consistent with the generation of more photo-carriers with increasing incident light intensity in the device. The photocurrent response of the devices as a function of applied bias voltages was also studied under a fixed incident light intensity and the results are presented in Fig. S12 in the ESI.† It shows that the photocurrent increases with increasing bias voltage because of an increase in the drift velocity of the photogenerated electrons and holes.

The photoresponsivity (R) is one of the key performance indicators for photodetectors, and is expressed as:

$$R = \frac{I_{ph}}{L_{light}} \quad (1)$$

where I_{ph} is the photocurrent and L_{light} is the incident light power. The active area of our typical photodetector is $\sim 7 \times 10^{-6}$ cm^2 (Fig. S10b, ESI†). The power dependent responsivity of the devices is plotted in Fig. 6. The highest responsivity of 54.5 mA W^{-1} was found for the $Cs_3Sb_2I_9$ film photodetector at a low intensity of incident light of 3.2 mW cm^{-2}, and R, drops quickly with increasing incident power to a steady value of ~ 28 mA W^{-1} with an illumination intensity of >30 mW cm^{-2}. For the $Cs_3Sb_2Br_9$ film photodetector, the highest responsivity is 3.6 mA W^{-1} at a low power density of 3.2 mW cm^{-2}, followed by a rapid drop with increasing illumination power density to a stable value of ~ 1.5 mA W^{-1} for a power intensity >20 mW cm^{-2}. For photoconductive photodetectors, the decrease in responsivity may be attributed to the saturation of surface states and deep defects filling along with an increase of the illumination power density.[55,56]

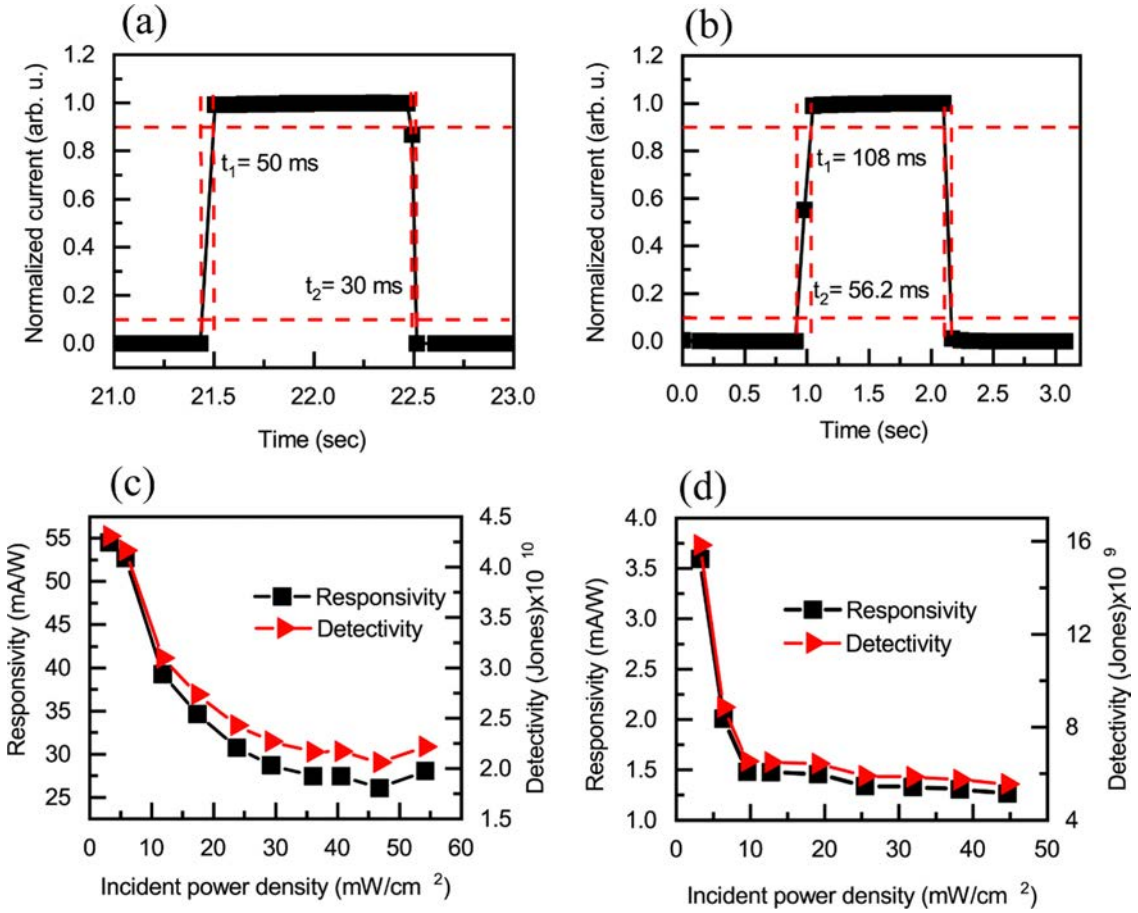

Fig. 6 Response time of (a) $Cs_3Sb_2I_9$ and (b) $Cs_3Sb_2I_9$ film photodetectors. Incident power dependent responsivity and detectivity of (c) $Cs_3Sb_2I_9$ and (d) $Cs_3Sb_2Br_9$ film photodetectors under the illumination of 532 and 450 nm light, respectively.

The photodetector detectivity (D^*), which characterizes the lowest level of light that it can operate, is evaluated according to the following expression:

$$D^* = \sqrt{\frac{A}{2qI_D}}R \quad (2)$$

where R is the responsivity, I_D is the dark current, q is the charge and A is the effective device area. Similar to the responsivity, as shown in Fig. 6(c) and (d), the maximum D^* at a low incident power density of 3.2 mW cm^{-2} is found to be 4.3×10^{10} Jones (cm $Hz^{1/2}$ W^{-1}) for the $Cs_3Sb_2I_9$ photodetector, which decreases to a stable value of $\sim 2 \times 10^{10}$ Jones at >30 mW cm^{-2} illumination power. Similarly, for the $Cs_3Sb_2Br_9$ photodetector, the maximum D^* is 1.6×10^{10} Jones at a low incident light intensity of 3.2 mW cm^{-2}, which decreases to a steady value of $\sim 6 \times 10^9$ Jones at >20 mW cm^{-2} incident power. The major performance parameters of film photodetector devices are compared with those of microplates in Table 1. In general, due to their higher crystallinity, the performance of microplate photodetectors is better than their film counterparts.

Unlike $Cs_3Sb_2I_9$, Table 1 shows that at 1 V bias the responsivity of the $Cs_3Sb_2I_9$ film photodetector is comparable to or even better than its microplate counterpart. In order to verify this, we also performed wavelength dependent photoresponse measurements, and the results are shown in Fig. S13 (ESI†). It can be seen that maximum responsivities of 26 mA W^{-1} at incident photons of wavelength ~ 575 nm and 8 mA W^{-1} at ~ 475 nm were obtained for the $Cs_3Sb_2I_9$ and $Cs_3Sb_2Br_9$ film devices, respectively. The responsivity then drops rapidly with increasing wavelength for both devices. The spectral responsivity follows the absorption characteristics and the exciton absorption edge of the corresponding thin films as depicted in Fig. 3(e and f). Comparing both thin film devices, as shown in Fig. 6(c and d) and also the wavelength dependent responsivity results,

Table 1 Comparison of the key performance parameters of CVD synthesized $Cs_3Sb_2X_9$ film photodetectors with their corresponding microplate photodetectors at an applied bias voltage of 1 V

Photodetector	Detection wavelength (nm)	Responsivity (mA W^{-1})	Detectivity (Jones)	Rise/decay time (ms)
$Cs_3Sb_2I_9$ microplate[46]	532	40	1.26×10^{11}	0.096/0.058
$Cs_3Sb_2I_9$ film	532	54.5	4.3×10^{10}	50/30
$Cs_3Sb_2Br_9$ microplate[48]	450	36.9	1.0×10^{10}	61.5/24
$Cs_3Sb_2Br_9$ film	450	3.6	1.6×10^{10}	108/56.2

the responsivity of the $Cs_3Sb_2Br_9$ film is lower than that of the $Cs_3Sb_2I_9$ film. This is consistent with the poorer film quality in terms of surface roughness and pinholes of the $Cs_3Sb_2Br_9$ film as revealed by the AFM and SEM images in Fig. 2 and Fig. S5 (ESI†). Note that the performance of $Cs_3Sb_2X_9$ film photodetectors reported in this work is not as good as those reported for other lead free all-inorganic halide perovskite thin films (namely, $Cs_3Cu_2I_5$ and $CsBi_2I_9$).[57–59] This may be attributed to the relatively rough films with high-density pinholes due to the relatively high temperature annealing process. We believe that the film quality can be improved by further optimizing the growth and annealing conditions.

Furthermore, the long-term compositional stability of the $Cs_3Sb_2X_9$ perovskite thin films and the performance stability of the film photodetectors were also studied. Fig. S14 (ESI†) shows a comparison of the XRD patterns of fresh $Cs_3Sb_2X_9$ film samples with films after storage in ambient air for 45 days without encapsulation. After storage, the obtained diffraction patterns are identical to the fresh annealed films, confirming the excellent phase stability in oxygen and moisture. However, a reduced diffraction peak intensity is observed which may indicate a degradation in crystallinity after storage. Fig. S15 and S16 (ESI†) show the photoresponse curves of the $Cs_3Sb_2X_9$ film photodetectors after 45 days of storage without encapsulation in ambient air. The photodetectors still show on/off photoswitching characteristics after 45 days of storage but with a slight degradation of photocurrent which may be associated with the crystallinity degradation observed in the XRD patterns after storage.

Conclusion

All-inorganic and Pb-free $Cs_3Sb_2X_9$ (X = I, Br) perovskite thin films have been synthesized successfully using a two-step CVD method. The obtained $Cs_3Sb_2I_9$ and $Cs_3Sb_2Br_9$ thin films show good crystallinity, and exhibit a large Stokes shift and high exciton binding energy. Refractive indices of 2.0 and 1.7 were obtained for $Cs_3Sb_2I_9$ and $Cs_3Sb_2Br_9$ thin films at their respective emission energies. The optical bandgaps were confirmed to be 2.2 and 2.85 eV for $Cs_3Sb_2I_9$ and $Cs_3Sb_2Br_9$ thin films. The films showed p-type semiconducting properties. Photoconductive devices fabricated from these films exhibit a commendable performance with responsivity values of up to 54.5 and 3.6 mA W^{-1} and high detectivity values reaching 4.3×10^{10} and 1.6×10^{10} Jones for $Cs_3Sb_2I_9$ and $Cs_3Sb_2Br_9$ film photodetectors, respectively. Moreover, a stable and reproducible photoswitching characteristic with fast rise and decay times of 50 ms and 30 ms, respectively, for $Cs_3Sb_2I_9$ and 108 ms and 56.2 ms, respectively for $Cs_3Sb_2Br_9$ film photodetectors were observed. The $Cs_3Sb_2X_9$ films exhibit excellent long-term stability even when stored without encapsulation in ambient air. The materials properties and overall photodetector performance suggest that $Cs_3Sb_2X_9$ perovskite thin films are also potential candidates similar to their microplate counterpart for future optoelectronic devices.

Experimental

Synthesis of $Cs_3Sb_2X_9$ thin films

A single-zone horizontal tube furnace (Hefei Kejing Materials Technology Co. Ltd., OTF-1200X) was used to synthesize $Cs_3Sb_2X_9$ thin films by a two-step CVD approach. Metal based CsI (99.9%) and SbI_3 (98%) from Sigma-Aldrich and CsBr (99.9%) and $SbBr_3$ (99.5%) from Alfa-Aesar were used as source materials. Similar procedures except for different conditions of vaporization temperature, pressure, and carrier gas flow rate were followed to synthesize $Cs_3Sb_2I_9$ and $Cs_3Sb_2Br_9$ thin films according to our previous reports on $Cs_3Sb_2X_9$ (X = I and Br) microplate synthesis.[46,48] Sapphire, glass and SiO_2 coated silicon (SiO_2/Si) substrates with dimensions of 40 mm × 10 mm were cleaned ultrasonically similar to that reported in ref. 46. The substrates were put 24 cm away from the center to the downstream side of the furnace. The vaporization of the source powder in the two steps was performed under optimized conditions of temperature and pressure and the carrier gas flow rate. Note that the total growth duration for each step of the two-step process was 10 minutes. Table 2 tabulates the optimized conditions of step I and step II depositions of the two-step CVD approach for growing $Cs_3Sb_2X_9$ perovskite thin films. Annealing of the as-grown samples was performed at 200 and 140 °C for 20 minutes at atmospheric pressure inside a tube furnace filled with N_2 gas to obtain $Cs_3Sb_2I_9$ and $Cs_3Sb_2Br_9$ thin films, respectively. The precursor powders of CsI and SbI_3, and CsBr and $SbBr_3$ were employed in a molar ratio of 1 : 3 and 1 : 6 to obtain a stoichiometric composition of $Cs_3Sb_2I_9$ and $Cs_3Sb_2Br_9$ thin films, respectively, in the two steps. Due to the very low melting temperature of SbX_3 compared to CsX, more SbX_3 precursor powder was needed to deposit a sufficient amount of SbX_3 materials over CsX. In order to achieve the final stoichiometric perovskite phase, a series of systematic optimization growth and annealing processes were performed with different precursor ratios. Some of the data from the systematic study are shown in Table S1 in the ESI.†

SE analysis

A J. A. Woollam RC2 ellipsometer was used for SE measurements. The measurements were carried out at incident angles of 55°, 65° and 75° using a rotating compensator in the energy range of 0.7 to 6.5 eV. The complex dielectric function of the films was obtained by fitting the SE spectra. A model comprising a three-layer structure, namely a surface roughness layer, a perovskite film, and a substrate, was used for data analysis. A numerical approximation (B-spline) was applied to estimate the

Table 2 Optimized parameters for the two-step CVD growth of $Cs_3Sb_2X_9$ perovskite thin films

Synthesis	Step	Source powder	Temperature (°C)	Pressure (Torr)	Flow rate (sccm)
$Cs_3Sb_2I_9$	Step I	CsI	550	2	200
	Step II	SbI_3	110	2	80
$Cs_3Sb_2Br_9$	Step I	CsBr	550	2	200
	Step II	$SbBr_3$	90	4	20

line shape of the dielectric functions and the thickness of the thin film. The film thickness was kept unchanged and the dielectric function parameters were considered as adjustable parameters. To obtain the best fitting of the experimentally obtained data, regression analysis was employed. Several Tauc–Lorentz oscillators were then applied to readjust the dielectric function according to the previous report.[60]

Photodetector fabrication

$Cs_3Sb_2X_9$ films were first deposited on a cleaned glass substrate by the above discussed CVD method. Au electrodes of ~40 nm thick were then deposited over the films using a shadow mask (Ni grids, 300 mesh) by thermal evaporation. The channel width and length of the device were 10 μm and 70 μm, respectively. A schematic diagram and optical image of the film photodetector device are shown in Fig. S10 (ESI†).

Characterization

The crystallinity and phase of $Cs_3Sb_2X_9$ perovskite thin films were investigated using a Bruker D2 Phaser diffractometer with Cu-Kα radiation (λ = 1.54184 Å). A Rigaku SmartLab X-ray diffractometer equipped with a Cu-Kα radiation source (λ = 1.54184 Å) was used for rocking curve measurements. The surface morphologies of the films were studied using a scanning electron microscope (JEOL JSM 820) and a Di Multi-Mode V (Veeco) AFM. The elemental composition of the perovskite thin films was obtained by X-ray fluorescence (XRF) spectroscopy using a Bruker S2 Puma system equipped with a palladium (Pd) anode. Room temperature photoluminescence (PL) spectroscopy was performed using a PL system comprising a 450 nm cw He–Cd laser, a collimator, an optical lens, and an ocean optics (USB 2000) spectrometer. The surface photovoltage (SPV) measurements of the thin films were performed by ambient pressure photoemission spectroscopy (APS) using a Kelvin Probe (APS04) instrument in the N_2-filled surface photovoltage spectrometer (SPS) module. Photodetector characterization was performed using a standard probe station with an Agilent 4155C semiconductor analyzer coupled with lasers (261 nm, 405 nm, 450 nm, 532 nm, 650 nm) as the excitation light source. A mechanical shutter was used to turn the illumination on and off on the device to characterize the photoswitching response of the devices.

Author contributions

Sujit Kumer Shil: carried out CVD growth, materials characterization, and photodetector testing, and wrote the manuscript draft. Fei Wang: carried out the photodetector testing. Kingsley O. Egbo: assisted in the materials characterization (spectroscopic ellipsometry). Ying Wang: assisted in the materials characterization (XRF). Cheuk Kai Gary Kwok: assisted in the materials characterization (SPV). Sai-Wing Tsang: provided assistance in the optical characterization (PL). Johnny C. Ho: provided assistance in the CVD growth. Kin Man Yu: supervised the research, assisted in data analysis, and edited the manuscript.

Conflicts of interest

The authors declare no competing financial interest.

Acknowledgements

This work was supported by the City University of Hong Kong SGP project No. 9380076, the Hong Kong Scholars Program (Grant No. XJ2019027), the General Research Fund (CityU 11306520), the Theme-based Research (T42-103/16-N) of the Research Grants Council of Hong Kong SAR, China, the Foshan Innovative and Entrepreneurial Research Team Program (No. 2018IT100031) and the National Natural Science Foundation of China (11874351).

References

1 M. Saliba, T. Matsui, K. Domanski, J.-Y. Seo, A. Ummadisingu, S. M. Zakeeruddin, J.-P. Correa-Baena, W. R. Tress, A. Abate, A. Hagfeldt and M. Grätzel, *Science*, 2016, **354**, 206–209.
2 D. Liu and T. L. Kelly, *Nat. Photonics*, 2014, **8**, 133–138.
3 A. Swarnkar, A. R. Marshall, E. M. Sanehira, B. D. Chernomordik, D. T. Moore, J. A. Christians, T. Chakrabarti and J. M. Luther, *Science*, 2016, **354**, 92–96.
4 E. M. Sanehira, A. R. Marshall, J. A. Christians, S. P. Harvey, P. N. Ciesielski, L. M. Wheeler, P. Schulz, L. Y. Lin, M. C. Beard and J. M. Luther, *Sci. Adv*, 2017, **3**, aao4204.
5 X. Hu, X. Zhang, L. Liang, J. Bao, S. Li, W. Yang and Y. Xie, *Adv. Funct. Mater.*, 2014, **24**, 7373–7380.
6 L. Dou, Y. M. Yang, J. You, Z. Hong, W. H. Chang, G. Li and Y. Yang, *Nat. Commun.*, 2014, **5**, 5404.
7 Y. Dong, Y. Gu, Y. Zou, J. Song, L. Xu, J. Li, J. Xue, X. Li and H. Zeng, *Small*, 2016, **12**, 5622–5632.
8 M. Shoaib, X. Wang, X. Zhang, X. Wang, H. Zhou, T. Xu, X. Hu, H. Liu, X. Fan, W. Zheng, T. Yang, S. Yang, Q. Zhang, X. Zhu, L. Sun and A. Pan, *J. Am. Chem. Soc.*, 2017, **139**, 15592–15595.
9 H. P. Wang, S. Li, X. Liu, Z. Shi, X. Fang and J. H. He, *Adv. Mater.*, 2021, **33**, 2003309.
10 Z. Q. Li, E. L. Hong, X. Y. Zhang, M. Deng and X. S. Fang, *J. Phys. Chem. Lett.*, 2022, **13**, 1215–1225.
11 Q. Zhang, R. Su, X. Liu, J. Xing, T. C. Sum and Q. Xiong, *Adv. Funct. Mater.*, 2016, **26**, 6238–6245.
12 B. Zhou, M. Jiang, H. Dong, W. Zheng, Y. Huang, J. Han, A. Pan and L. Zhang, *ACS Photonics*, 2019, **6**, 793–801.
13 Y. Tong, E. P. Yao, A. Manzi, E. Bladt, K. Wang, M. Döblinger, S. Bals, P. Müller-Buschbaum, A. S. Urban, L. Polavarapu and J. Feldmann, *Adv. Mater.*, 2018, **30**, 1801117.
14 J. Pan, L. N. Quan, Y. Zhao, W. Peng, B. Murali, S. P. Sarmah, M. Yuan, L. Sinatra, N. M. Alyami, J. Liu, E. Yassitepe, Z. Yang, O. Voznyy, R. Comin, M. N. Hedhili, O. F. Mohammed, Z. H. Lu,

D. H. Kim, E. H. Sargent and O. M. Bakr, *Adv. Mater.*, 2016, **28**, 8718–8725.
15 X. Du, G. Wu, J. Cheng, H. Dang, K. Ma, Y. W. Zhang, P. F. Tan and S. Chen, *RSC Adv.*, 2017, **7**, 10391–10396.
16 K. Lin, J. Xing, L. N. Quan, F. P. G. de Arquer, X. Gong, J. Lu, L. Xie, W. Zhao, D. Zhang, C. Yan, W. Li, X. Liu, Y. Lu, J. Kirman, E. H. Sargent, Q. Xiong and Z. Wei, *Nature*, 2018, **562**, 245–248.
17 C. R. Kagan, D. B. Mitzi and C. D. Dimitrakopoulos, *Science*, 1999, **286**, 945–947.
18 L. Zhu, H. Zhang, Q. Lu, Y. Wang, Z. Deng, Y. Hu, Z. Lou, Q. Cui, Y. Hou and F. Teng, *J. Mater. Chem. C*, 2018, **6**, 3945–3950.
19 Y. F. Xu, M. Z. Yang, B. X. Chen, X. D. Wang, H. Y. Chen, D. Bin Kuang and C. Y. Su, *J. Am. Chem. Soc.*, 2017, **139**, 5660–5663.
20 G. Gao, Q. Xi, H. Zhou, Y. Zhao, C. Wu, L. Wang, P. Guo and J. Xu, *Nanoscale*, 2017, **9**, 12032–12038.
21 A. Kojima, K. Teshima, Y. Shirai and T. Miyasaka, *J. Am. Chem. Soc.*, 2009, **131**, 6050–6051.
22 M. Kim, J. Jeong, H. Lu, T. K. Lee, F. T. Eickemeyer, Y. Liu, I. W. Choi, S. J. Choi, Y. Jo, H. B. Kim, S. I. Mo, Y. K. Kim, H. Lee, N. G. An, S. Cho, W. R. Tress, S. M. Zakeeruddin, A. Hagfeldt, J. Y. Kim, M. Grätzel and D. S. Kim, *Science*, 2022, **375**, 302–306.
23 W. Deng, X. Xu, X. Zhang, Y. Zhang, X. Jin, L. Wang, S. T. Lee and J. Jie, *Adv. Funct. Mater.*, 2016, **26**, 4797–4802.
24 Y. Ling, Z. Yuan, Y. Tian, X. Wang, J. C. Wang, Y. Xin, K. Hanson, B. Ma and H. Gao, *Adv. Mater.*, 2016, **28**, 305–311.
25 Y. Yuan and J. Huang, *Acc. Chem. Res.*, 2016, **49**, 286–293.
26 B. Luo, Y. C. Pu, S. A. Lindley, Y. Yang, L. Lu, Y. Li, X. Li and J. Z. Zhang, *Angew. Chem., Int. Ed.*, 2016, **55**, 8864–8868.
27 D. P. Nenon, J. A. Christians, L. M. Wheeler, J. L. Blackburn, E. M. Sanehira, B. Dou, M. L. Olsen, K. Zhu, J. J. Berry and J. M. Luther, *Energy Environ. Sci.*, 2016, **9**, 2072–2082.
28 H. Huang, M. I. Bodnarchuk, S. V. Kershaw, M. V. Kovalenko and A. L. Rogach, *ACS Energy Lett.*, 2017, **2**, 2071–2083.
29 S. F. Hoefler, G. Trimmel and T. Rath, *Monatsh. Chem.*, 2017, **148**, 795–826.
30 T. C. Jellicoe, J. M. Richter, H. F. J. Glass, M. Tabachnyk, R. Brady, S. E. Dutton, A. Rao, R. H. Friend, D. Credgington, N. C. Greenham and M. L. Böhm, *J. Am. Chem. Soc.*, 2016, **138**, 2941–2944.
31 X. Wu, W. Song, Q. Li, X. Zhao, D. He and Z. Quan, *Chem. – Asian J.*, 2018, **13**, 1654–1659.
32 J. P. Correa-Baena, L. Nienhaus, R. C. Kurchin, S. S. Shin, S. Wieghold, N. T. Putri Hartono, M. Layurova, N. D. Klein, J. R. Poindexter, A. Polizzotti, S. Sun, M. G. Bawendi and T. Buonassisi, *Chem. Mater.*, 2018, **30**, 3734–3742.
33 A. Singh, K. M. Boopathi, A. Mohapatra, Y. F. Chen, G. Li and C. W. Chu, *ACS Appl. Mater. Interfaces*, 2018, **10**, 2566–2573.
34 F. Umar, J. Zhang, Z. Jin, I. Muhammad, X. Yang, H. Deng, K. Jahangeer, Q. Hu, H. Song and J. Tang, *Adv. Opt. Mater.*, 2019, **7**, 1801368.
35 B. Ghosh, S. Chakraborty, H. Wei, C. Guet, S. Li, S. Mhaisalkar and N. Mathews, *J. Phys. Chem. C*, 2017, **121**, 17062–17067.
36 Y. Zhang, J. Yin, M. R. Parida, G. H. Ahmed, J. Pan, O. M. Bakr, J. L. Brédas and O. F. Mohammed, *J. Phys. Chem. Lett.*, 2017, **8**, 3173–3177.
37 M. Lyu, J. H. Yun, M. Cai, Y. Jiao, P. V. Bernhardt, M. Zhang, Q. Wang, A. Du, H. Wang, G. Liu and L. Wang, *Nano Res.*, 2016, **9**, 692–702.
38 B. Ghosh, B. Wu, H. K. Mulmudi, C. Guet, K. Weber, T. C. Sum, S. Mhaisalkar and N. Mathews, *ACS Appl. Mater. Interfaces*, 2018, **10**, 35000–35007.
39 T. Singh, A. Kulkarni, M. Ikegami and T. Miyasaka, *ACS Appl. Mater. Interfaces*, 2016, **8**, 14542–14547.
40 B. Saparov, F. Hong, J. P. Sun, H. S. Duan, W. Meng, S. Cameron, I. G. Hill, Y. Yan and D. B. Mitzi, *Chem. Mater.*, 2015, **27**, 5622–5632.
41 C. Lu, D. S. Itanze, A. G. Aragon, X. Ma, H. Li, K. B. Ucer, C. Hewitt, D. L. Carroll, R. T. Williams, Y. Qiu and S. M. Geyer, *Nanoscale*, 2020, **12**, 2987–2991.
42 Z. Ma, Z. Shi, D. Yang, F. Zhang, S. Li, L. Wang, D. Wu, Y. Zhang, G. Na, L. Zhang, X. Li, Y. Zhang and C. Shan, *ACS Energy Lett.*, 2020, 385–394.
43 Z. Zheng, Q. Hu, H. Zhou, P. Luo, A. Nie, H. Zhu, L. Gan, F. Zhuge, Y. Ma, H. Song and T. Zhai, *Nanoscale Horizons*, 2019, **4**, 1372–1379.
44 P. Liu, Y. Liu, S. Zhang, J. Li, C. Wang, C. Zhao, P. Nie, Y. Dong, X. Zhang, S. Zhao and G. Wei, *Adv. Opt. Mater.*, 2020, **2001072**, 1–9.
45 D. Pan, Y. Fu, J. Chen, K. J. Czech, J. C. Wright and S. Jin, *Nano Lett.*, 2018, **18**, 1807–1813.
46 S. K. Shil, F. Wang, Z. Lai, Y. Meng, Y. Wang, D. Zhao, M. K. Hossain, K. O. Egbo, Y. Wang, K. M. Yu and J. C. Ho, *Nano Res.*, 2021, **14**, 4116–4124.
47 P. Kristin, DOI: **10.17188/1264913**.
48 S. K. Shil, F. Wang, K. O. Egbo, Z. Lai, Y. Wang, Y. Wang, D. Zhao, S.-W. Tsang, J. C. Ho and K. M. Yu, *ACS Appl. Mater. Interfaces*, 2021, **13**, 35930–35940.
49 A. M. A. Leguy, P. Azarhoosh, M. I. Alonso, M. Campoy-Quiles, O. J. Weber, J. Yao, D. Bryant, M. T. Weller, J. Nelson, A. Walsh, M. Van Schilfgaarde and P. R. F. Barnes, *Nanoscale*, 2016, **8**, 6317–6327.
50 J. S. Manser, J. A. Christians and P. V. Kamat, *Chem. Rev.*, 2016, **116**, 12956–13008.
51 B. Yang, L. Yin, G. Niu, J. H. Yuan, K. H. Xue, Z. Tan, X. S. Miao, M. Niu, X. Du, H. Song, E. Lifshitz and J. Tang, *Adv. Mater.*, 2019, **31**, 1904711.
52 H. Dammak, A. Yangui, S. Triki, Y. Abid and H. Feki, *J. Lumin.*, 2015, **161**, 214–220.
53 A. Swarnkar, R. Chulliyil, V. K. Ravi, M. Irfanullah, A. Chowdhury and A. Nag, *Angew. Chem., Int. Ed.*, 2015, **54**, 15424–15428.
54 I. Vázquez-Fernández, S. Mariotti, O. S. Hutter, M. Birkett, T. D. Veal, T. D. C. Hobson, L. J. Phillips, L. Danos, P. K. Nayak, H. J. Snaith, W. Xie, M. P. Sherburne, M. Asta and K. Durose, *Chem. Mater.*, 2020, **32**, 6676–6684.
55 M. Gong, R. Sakidja, R. Goul, D. Ewing, M. Casper, A. Stramel, A. Elliot and J. Z. Wu, *ACS Nano*, 2019, **13**, 1772–1783.
56 G. Konstantatos, J. Clifford, L. Levina and E. H. Sargent, *Nat. Photonics*, 2007, **1**, 531–534.

57 Z. X. Zhang, C. Li, Y. Lu, X. W. Tong, F. X. Liang, X. Y. Zhao, D. Wu, C. Xie and L. B. Luo, *J. Phys. Chem. Lett.*, 2019, **10**, 5343–5350.
58 W. G. Li, X. D. Wang, J. F. Liao, Y. Jiang and D. Bin Kuang, *Adv. Funct. Mater.*, 2020, **30**, 1909701.
59 Z. Li, X. Liu, C. Zuo, W. Yang and X. Fang, *Adv. Mater.*, 2021, **33**, 2103010.
60 K. O. Egbo, C. P. Liu, M. K. Hossain, C. Y. Ho, C. G. Kwok, S. K. Shil, C. V. Ezeh, Y. Wang and K. M. Yu, *J. Phys. Chem. C*, 2020, **124**, 20000–20009.